AGU PUBLICATIONS

Journal of Geophysical Research: Space Physics

RESEARCH ARTICLE

10.1002/2014JA020366

Electron losses from the radiation belts caused by EMIC waves

Tobias Kersten[1], **Richard B. Horne**[1], **Sarah A. Glauert**[1], **Nigel P. Meredith**[1],
Brian J. Fraser[2], **and Russell S. Grew**[2]

[1]British Antarctic Survey, Natural Environment Research Council, Cambridge, UK, [2]Centre for Space Physics, University of Newcastle, Newcastle, New South Wales, Australia

Key Points:

- EMIC waves cause electron loss for pitch angles < 60° and energies > 2 MeV
- The distribution left behind in space is a pancake distribution at E > 6 MeV
- EMIC waves are unlikely to set an upper energy limit on the electron flux

Correspondence to:
T. Kersten,
tobker@bas.ac.uk

Citation:
Kersten, T., R. B. Horne, S. A. Glauert, N. P. Meredith, B. J. Fraser, and R. S. Grew (2014), Electron losses from the radiation belts caused by EMIC waves, *J. Geophys. Res. Space Physics*, *119*, 8820–8837, doi:10.1002/2014JA020366.

Received 4 JUL 2014
Accepted 8 OCT 2014

Abstract Electromagnetic Ion Cyclotron (EMIC) waves cause electron loss in the radiation belts by resonating with high-energy electrons at energies greater than about 500 keV. However, their effectiveness has not been fully quantified. Here we determine the effectiveness of EMIC waves by using wave data from the fluxgate magnetometer on CRRES to calculate bounce-averaged pitch angle and energy diffusion rates for $L^* = 3.5$–7 for five levels of *Kp* between 12 and 18 MLT. To determine the electron loss, EMIC diffusion rates were included in the British Antarctic Survey Radiation Belt Model together with whistler mode chorus, plasmaspheric hiss, and radial diffusion. By simulating a 100 day period in 1990, we show that EMIC waves caused a significant reduction in the electron flux for energies greater than 2 MeV but only for pitch angles lower than about 60°. The simulations show that the distribution of electrons left behind in space looks like a pancake distribution. Since EMIC waves cannot remove electrons at all pitch angles even at 30 MeV, our results suggest that EMIC waves are unlikely to set an upper limit on the energy of the flux of radiation belt electrons.

1. Introduction

In the Van Allen radiation belts high-energy electrons are circulating around the Earth trapped by Earth's magnetic field. The inner electron belt is located close to the Earth ranging from about $L = 1.2$ to $L = 2$. The outer electron belt extends from about $L = 3$ to $L = 7$ and beyond, depending on geomagnetic activity. The belts contain electrons with energies ranging from about 100 keV to several MeV. In contrast to the inner belt the electron fluxes in the outer belt are highly variable [*Paulikas and Blake*, 1979; *Baker et al.*, 1986]. *Baker et al.* [2013] have recently discovered a narrow third radiation belt that persisted for about 4 weeks, consisting of ultrarelativistic electrons with energies as high as 5.6 MeV, showing that knowledge about the high-energy structure of the radiation belts is still evolving.

One of the long outstanding problems in magnetospheric physics is to understand and predict the variability and formation of the outer electron belt. Two of the most important processes for this are the radial diffusion of electrons and electron acceleration and loss caused by interactions between electrons and plasma waves. Radial diffusion of particles across the field is driven by ultra low frequency (ULF) waves assuming conservation of the first and second adiabatic invariants. As a result, if particles are diffused toward the Earth the energy will increase. Data from the Van Allen Probes mission suggest that the distribution of the electron phase space density allows for radial diffusion toward the Earth at about $L^* < 5.5$ and away from the Earth outside L^* of 5.5 [*Reeves et al.*, 2013]. Therefore, radial diffusion can also act as a loss process, if electrons are diffused out to the magnetopause, e.g., *Shprits et al.* [2006].

Up until about the late 1990s, it was believed that radial diffusion was the main driver of the variability of the outer electron belt. However, it has been shown that wave-particle interactions also play an important role in electron acceleration and loss [*Summers et al.*, 1998; *Horne and Thorne*, 1998]. There is a variety of different plasma waves involved, including chorus, magnetosonic waves, plasmaspheric hiss, and EMIC waves.

Chorus waves are discrete whistler mode emissions generated by cyclotron resonant interactions with suprathermal electrons [*Katoh and Omura*, 2007; *Li et al.*, 2008], which are injected into the inner magnetosphere during (sub)storms. They are a major process for acceleration and loss of relativistic electrons [*Horne et al.*, 2005a, 2005b]. For example, they are thought to be largely responsible for the buildup of the radiation belts during the recovery phase of storms [*Horne et al.*, 2005a, 2006]. Chorus waves at high latitudes are also thought to cause microburst precipitation and thereby lead to losses of electrons in the radiation belts [*Lorentzen et al.*, 2001]. Both, the diffuse and the pulsating aurora are mainly caused by pitch angle scattering by whistler mode chorus waves [*Thorne et al.*, 2010; *Nishimura et al.*, 2010]. Chorus waves tend to be most significant outside the plasmapause on the dawnside during active conditions [*Meredith et al.*, 2001, 2012; *Li et al.*, 2011].

Magnetosonic waves may also lead to local acceleration and may particularly energize electrons with energies between 10 keV up to a few MeV in the outer radiation belt [*Horne et al.*, 2007]. They are thought to be generated by proton ring distributions at energies of about 10 keV [*Boardsen et al.*, 1992] and can propagate both inside and outside the plasmapause [*Meredith et al.*, 2008; *Ma et al.*, 2013].

Inside the plasmapause, plasmaspheric hiss acts as an important loss process, since the formation of the slot region between the inner and the outer radiation belt is mainly due to resonant pitch angle scattering of energetic electrons with plasmaspheric hiss [*Lyons and Thorne*, 1973; *Meredith et al.*, 2007, 2009]. Furthermore, resonant wave-particle interactions with plasmaspheric hiss contribute to electron loss in the outer radiation belt [*Summers et al.*, 2007; *Meredith et al.*, 2006].

Below the proton cyclotron frequency waves known as Electromagnetic Ion Cyclotron (EMIC) waves have been suggested as an important loss process [*Horne and Thorne*, 1998]. They can cause electron loss in the radiation belts, when their frequency is Doppler shifted to the electron cyclotron frequency by the relative motion of the waves and electrons along the field line. This enables the EMIC waves to resonate with high-energy electrons at energies greater than about 500 keV [*Meredith et al.*, 2003] and thereby causing losses due to pitch angle scattering into the loss cone. It has been suggested by *Cornwall et al.* [1970] that EMIC waves are generated close to the equator by a temperature anisotropy in the energetic proton distribution at energies of a few tens of keV to 100 keV, which are typical for ring current ions. They are categorized into three frequency bands: Hydrogen band waves have a frequency between the proton cyclotron frequency f_{cp} and the helium ion cyclotron frequency f_{cHe}. Helium band waves have a frequency between the oxygen and the helium ion cyclotron frequency. Waves with a frequency below the oxygen ion cyclotron frequency are difficult to detect against a noisy background and rarely observed. EMIC waves in different bands can have different spectral properties and therefore a different effect on the electron distribution.

It has been shown that for amplitudes of approximately 1 nT and more EMIC waves cause strong pitch angle scattering and are able to diffuse electrons into the loss cone very effectively [*Summers and Thorne*, 2003] at energies greater than about 1–2 MeV [*Albert*, 2003; *Summers and Thorne*, 2003] and therefore may contribute significantly to the decay of the radiation belts [*Horne and Thorne*, 1998]. However, these losses have not been fully quantified. The purpose of this study is to assess the role of the EMIC waves and their importance as a loss process for the radiation belts. In order to do this, we use the results of the companion paper [*Meredith et al.*, 2014a], which presents the global morphology and spectral properties of EMIC waves derived from CRRES observations, to calculate pitch angle and energy diffusion rates and incorporate them in the British Antarctic Survey (BAS) Radiation Belt Model. To assess the importance of EMIC waves on a global scale, the model is applied to a 100 day period measured by CRRES.

We will begin with a brief introduction of the BAS Radiation Belt Model and the Pitch Angle and energy Diffusion of Ions and Electrons (PADIE) code (section 2), followed by a description of the EMIC wave database and the nominal wave model in section 3. We will then present our results for the diffusion coefficients (section 4) and of the global simulations (section 5). The results are discussed and the conclusions are presented in sections 6 and 7, respectively.

2. The BAS Radiation Belt Model and the PADIE Code

To model the radiation belts, we use the BAS Radiation Belt Model [*Glauert et al.*, 2014], which solves the Fokker-Planck equation to calculate the change in the electron phase space density f for a given location, particle energy, pitch-angle, and time:

$$\frac{\partial f}{\partial t} = \frac{1}{g(\alpha)}\frac{\partial}{\partial \alpha}\bigg|_{E,L}\left(g(\alpha)D_{\alpha\alpha}\frac{\partial f}{\partial \alpha}\bigg|_{E,L}\right) + \frac{1}{A(E)}\frac{\partial}{\partial E}\bigg|_{\alpha,L}\left(A(E)D_{\mathrm{EE}}\frac{\partial f}{\partial E}\bigg|_{\alpha,L}\right) + L^2\frac{\partial}{\partial L}\bigg|_{\mu,J}\left(\frac{D_{\mathrm{LL}}}{L^2}\frac{\partial f}{\partial L}\bigg|_{\mu,J}\right) - \frac{f}{\tau_L}$$

Here the first term describes diffusion in pitch angle, the second diffusion in energy, the third radial diffusion, and the last term describes the losses to the atmosphere, which only applies inside the loss cone. Each term is described by *Glauert et al.* [2014]. In particular, the Fokker-Planck equation depends on the drift and bounce-averaged diffusion coefficients for radial diffusion (D_{LL}), pitch angle diffusion ($D_{\alpha\alpha}$), and energy diffusion (D_{EE}), which depend on location, particle energy, pitch angle, and magnetic activity. They are computed using the PADIE diffusion code [*Glauert and Horne*, 2005], which calculates the diffusion coefficients based on quasi-linear theory. The PADIE code assumes a Gaussian distribution of the wave power in frequency and therefore the peak frequency and width of the Gaussian need to be specified. As explained in detail in *Glauert et al.* [2014], the Fokker-Planck equation requires to define boundaries for the pitch angle, energy, and L^*. Here we have used a pitch angle ranging from 0° to 90° with a minimum energy of $E_{min} = 153$ keV at $L^* = 2.05$ and a maximum energy of $E_{max} = 20$ MeV at $L^* = 5.55$. The minimum and maximum values of L^* have been set to $L^*_{min} = 2.05$ and $L^*_{max} = 5.55$.

The first code to solve the three-dimensional Fokker-Planck equation was developed by *Beutier and Boscher* [1995] for high-energy radiation belt electrons. *Varotsou et al.* [2005] showed that chorus waves can cause electron acceleration and loss by including data from the CRRES mission at low latitudes up to 15° into the model of Beutier and Boscher. This model was then extended to latitudes up to 30° by *Albert et al.* [2009]. *Subbotin and Shprits* [2009] presented the Versatile Electron Radiation Belts (VERB) code, which utilizes parameterized diffusion models to include the effect of chorus, plasmaspheric hiss, and EMIC waves. A similar model using the same parameterized wave models was developed by *Su et al.* [2010]. Four-dimensional models that include the effect of wave-particle interactions have been developed by *Jordanova et al.* [2008] and *Fok et al.* [2008]. The numerical scheme used in the BAS Radiation Belt Model is similar to the one employed by the VERB code but with new models for the wave-particle interactions.

The BAS Radiation Belt Model includes radial transport exploiting the radial diffusion coefficients of *Brautigam and Albert* [2000]. Furthermore, it includes wave-particle interactions due to whistler mode chorus waves based on a new chorus diffusion matrix [*Horne et al.*, 2013] and—inside the plasmasphere—plasmaspheric hiss based on *Meredith et al.* [2004].

The models for the global simulation of the radiation belts require drift and bounce-averaged pitch angle and energy diffusion coefficients. For three-dimensional models these are computed using quasi-linear theory. Although, particularly, chorus waves are known to be highly nonlinear due to their short-duration rising tone frequency structure [e.g., *Omura et al.*, 2009; *Santolík et al.*, 2014], it is not yet computationally feasible to simulate chorus waves using nonlinear models over the duration and spatial dimensions required by global models. It has been demonstrated by *Albert* [2010] and *Tao et al.* [2012] that there is remarkable agreement between fully nonlinear and quasi-linear simulations for waves with a wave power less than about 0.5 nT.

3. Calculating EMIC Diffusion Rates

3.1. EMIC Wave Database

To calculate the diffusion rates, data from a database of EMIC waves measured by the CRRES satellite were used. Since details of the database are given in the companion paper [*Meredith et al.*, 2014a], only a short summary is given here. The database contains the peak spectral intensity, the frequency of the peak spectral intensity, from now on referred to as peak frequency f_m, the spectral width df, and the wave intensity integrated over the wave band, obtained by a Gaussian fit to the wave data from 830 identified EMIC wave event intervals. The data are separated into the hydrogen and helium frequency band. The CRRES satellite operated in a highly elliptical (350 × 35,548 km) geosynchronous transfer orbit with a low inclination (18.1°). Because of its orbital coverage, EMIC wave events were identified in the range of $L^* = 3.5–7.0$, with a gap in the prenoon sector. For each spectral profile the satellite position in magnetic coordinates (L^*, MLT, λ_m) together with the proton gyrofrequency f_{cp}, the plasma frequency f_{ce}, and the magnetic activity as given by the *Kp* index was stored at the 25.6 s resolution of the data set, irrespective of whether EMIC waves were present or not. The coordinates were computed using the Office National d'Etudes et de Recherche Aérospatiales - Département Environnement Spatial (ONERA-DESP) library V4.2 [*Boscher and Bourdarie*, 2004], using the International Geomagnetic Reference Field at the middle of the appropriate year and the Olson-Pfitzer quiet time model [*Olson and Pfitzer*, 1977]. There are several time-dependent external magnetic field models that can be used to represent active conditions but large uncertainties remain during very disturbed periods [e.g., *McCollough et al.*, 2008] and most require solar wind parameters which are not fully available for the CRRES mission. We use the Olson-Pfitzer quiet time model because it has been shown to be a good-average external magnetic field model when compared to measurements [*Friedel et al.*, 2005] and has recently been adopted by the Panel for Radiation Belt Environment Modeling for improving space radiation models. Since the software is designed for particles and we are applying it to waves, we assume a local

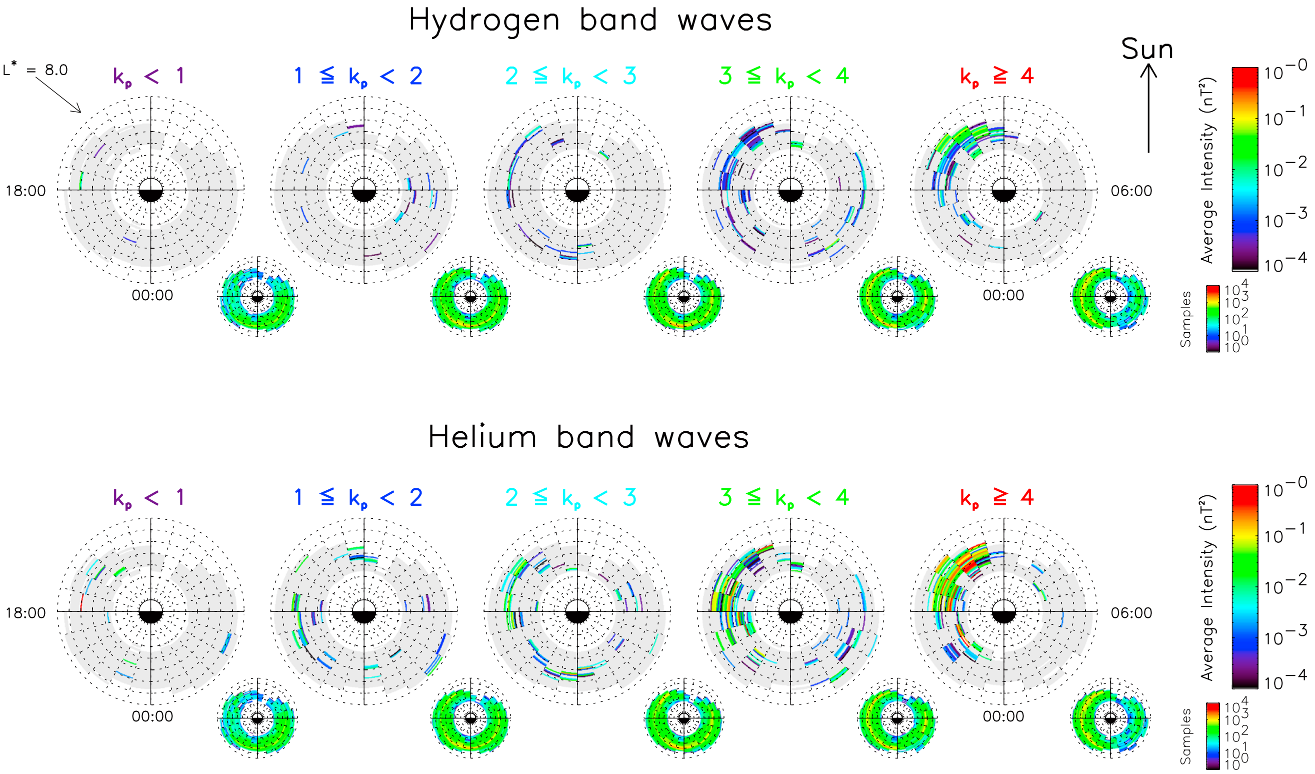

Figure 1. Average wave intensities of (top) hydrogen band and (bottom) helium band EMIC waves as a function of L^* and MLT for (left to right) increasing levels of geomagnetic activity as monitored by the *Kp* index. In both Figures 1 (top) and 1 (bottom), the average intensities are shown in the large plots and the corresponding sample distribution in the small plots.

pitch angle of 90° in the calculation of L^*. Further details about the processing of the data can be found in the companion paper [*Meredith et al.*, 2014a].

3.2. Spectral Properties and Nominal Model

The data were initially arranged into 24 MLT bins, five levels of magnetic activity ($Kp < 1$, $1 \leq Kp < 2$, $2 \leq Kp < 3$, $3 \leq Kp < 4$, $Kp \geq 4$), and seven bins of L^* with a size of $0.1L^*$ ranging from $L^* = 3.0$ to $L^* = 7.0$. Due to the limited orbital coverage and instrumental sensitivity, EMIC wave events could only be found in this region by CRRES. This study thereby excludes EMIC waves at higher L^*, as found by, e.g., *Anderson et al.* [1992a] and *Usanova et al.* [2012]. The time-averaged intensities of the hydrogen and helium band EMIC waves as a function of L^*, MLT, and magnetic activity are shown in Figure 1. Here the average intensities are shown in the large plots and the corresponding sampling distribution in the small plots, while the grey area in the large plots was sampled by CRRES but no EMIC waves were detected. The majority of the strongest EMIC waves occur in the afternoon sector (12–18 MLT) with average intensities up to about 0.5 nT^2. They are found for all L^*, but in particular for $5 < L^* < 6$. There are only an insignificant number of events outside the afternoon sector, with most of them having a weak wave power compared to the events in the afternoon sector. Note that the intensities and the occurrence rate of EMIC waves increase with magnetic activity and also helium band waves are generally stronger than hydrogen band waves.

A previous analysis of Active Magnetospheric Particle Tracer Explorers (AMPTE) data found that the average power spectral density typically lies between 1 and 10 nT^2 Hz^{-1} [*Anderson et al.*, 1992a, 1992b] with a peak-to-peak wave amplitude of about 2.5 nT^2. The CRRES results reveal that the peak power spectral density typically lies between 1 and 100 nT^2/Hz and may also reach 1000 nT^2/Hz for the helium band [*Meredith et al.*, 2014a]. The peak wave intensities can reach up to about 10 nT^2 occasionally and are therefore a little higher but generally agree with the AMPTE observations.

3.2.1. Characteristic Frequencies

Since the number of events of the resulting global EMIC wave database is sparse, we decided to define a nominal EMIC wave model based on the global database. Therefore, we analyzed the frequency spectra

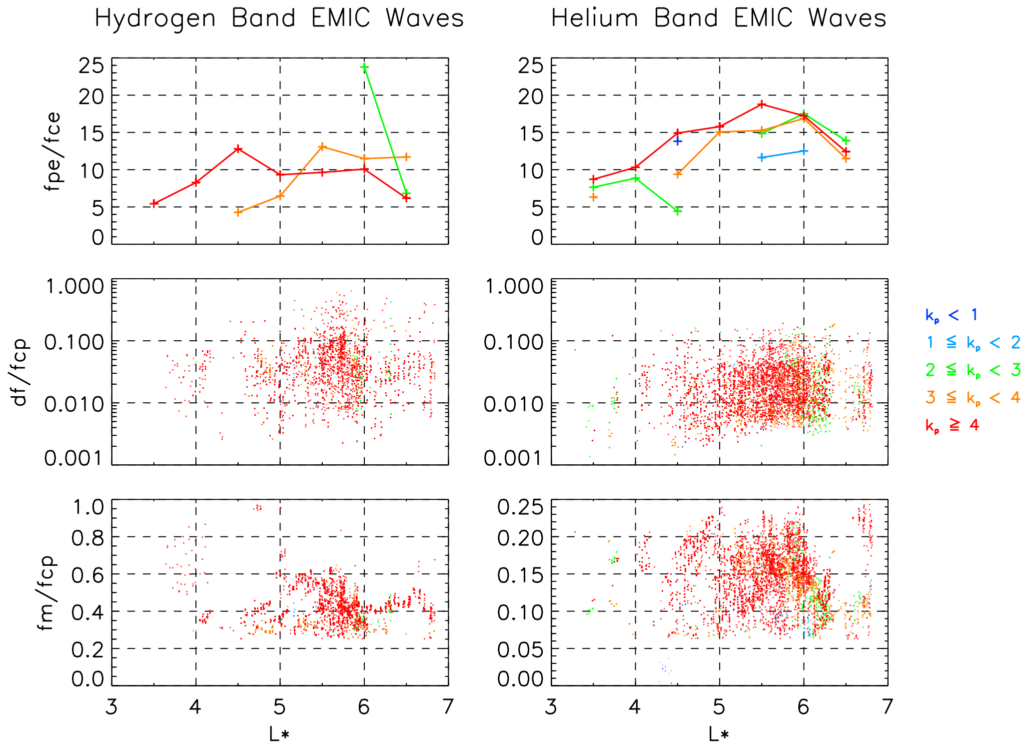

Figure 2. Line plots of the ratio of (top) f_{pe}/f_{ce} and scatterplots of (middle) the normalized frequency width df/f_{cp} and (bottom) the normalized peak frequency f_m/f_{cp} for all hydrogen band (left column) and helium band (right column) EMIC events with an intensity greater than 0.1 nT^2.

of the hydrogen and helium band EMIC waves separately. In this process only waves in the afternoon sector with a peak power spectral density above a threshold of 0.1 nT^2 were taken into account, in order to build the nominal model based only on waves with significant wave power. Figure 2 shows scatterplots of the normalized peak frequency (f_m/f_{cp}), normalized frequency width (df/f_{cp}), and the ratio of the electron plasma frequency to the electron cyclotron frequency (f_{pe}/f_{ce}) for all considered hydrogen and helium band EMIC events.

For the hydrogen band EMIC events (left column), the peak frequency varies from $f_m/f_{cp} \approx 0.25$ to $f_m/f_{cp} \approx 0.6$ with most events close to $f_m/f_{cp} = 0.4$. There is no obvious variation with *Kp*. Therefore, we decided to set the peak frequency of hydrogen band EMIC waves to $f_m/f_{cp} = 0.4$.

The frequency width can vary by an order of magnitude from $df/f_{cp} = 0.01$ to $df/f_{cp} = 0.1$ with also no clear trend in *Kp*. In order to ensure that the wave power does not extend into the cutoff frequency (see below), we have chosen $df/f_{cp} = 0.02$ as a representative value.

For helium band waves (right column) f_m/f_{cp} is spread from the lower to the upper frequency limit of the helium band, i.e., from 0.0625 to 0.25. The width of the spectrum also varies considerably. To represent these waves in the nominal model, we have chosen to set $f_m/f_{cp} = 0.15$ and $df/f_{cp} = 0.02$ which lie in the middle range of our observations.

In the nominal model we also need to specify the lower and upper cutoff frequencies outside which the wave power is set to zero. Since a Gaussian power spectrum falls off rapidly with frequency, we have set the lower and upper cutoffs to be twice the bandwidth, for both hydrogen and helium band waves.

3.2.2. The Ratio of f_{pe}/f_{ce}

The ratio of the plasma frequency to the electron cyclotron frequency f_{pe}/f_{ce} is known to be an important parameter that is proportional to the square root of the plasma density and also defines the resonant energy at which electron diffusion will likely be most effective. While the hydrogen band waves show some variation in f_{pe}/f_{ce} with most events occurring around $f_{pe}/f_{ce} = 10$, the spread for helium band waves is much higher, ranging from about $6 < f_{pe}/f_{ce} < 19$, with most values clustered around $f_{pe}/f_{ce} = 15$. The ratio of f_{pe}/f_{ce} used in our chorus model, which will be combined with these data for the global simulations, however, is clustered around $f_{pe}/f_{ce} = 10$. Since we want to study the effects of EMIC waves while chorus is present, the EMIC plasma densities need to be consistent with the chorus density model, which is around $f_{pe}/f_{ce} = 10$, if averaged over the afternoon sector. Therefore, we have set $f_{pe}/f_{ce} = 10$ for the nominal model for both, hydrogen and helium band waves. The effects of the ratio of f_{pe}/f_{ce} on the EMIC waves are discussed in the discussion section, showing that the results presented here are robust.

3.2.3. Wave Normal Angle

The wave normal angle ψ is the angle between the k vector of the wave and the ambient magnetic field. The PADIE code, used to calculate the diffusion coefficients, assumes a Gaussian distribution in X, where $X = \tan\,\psi$, for the wave normal angle. Information about the wave normal angle of EMIC waves is very limited. Wave polarization experiments have shown that near the equator the waves are a mixture ranging from left hand circularly polarized waves to highly elliptical or linear polarized waves, whereas at higher latitudes the waves become more linearly polarized [*Anderson et al.*, 1992b]. This either suggests that the waves are not strictly field aligned or that there is a distribution of field-aligned circular polarized waves propagating away from the equator and a second distribution that has been reflected at high latitudes and has a large wave normal angle and could account for the linear polarization at the equator [*Horne and Thorne*, 1994].

In order to provide a mixture of circular and linear polarization, we have chosen to set the Gaussian distribution of the wave normal angle in the nominal model for EMIC waves to be peaked in the field-aligned direction, i.e., $X_m = \tan\,0° = 0$, with a width of $X_w = \tan\,15°$. To include most of the wave power, we have set the cutoffs in X to $X_{cut} = 2X_w$ outside of which the wave power is set to zero.

3.2.4. Ion Composition

The ion composition of the plasma sets limits on the characteristic wave frequencies of a multi-ion plasma and hence constrains EMIC waves. Thus, the ion composition is a very important parameter. Unfortunately, it is very difficult to measure in space, since the ion distribution is dominated by thermal ions with energies of about 1 eV. Spacecraft plasma detectors in this energy region are hindered by sheath effects around the spacecraft and by problems associated with the spacecraft potential. Previous studies have estimated an ion composition with a helium fraction between 5 and 10 % and also 5 and 10 % O^+, with the rest being hydrogen ions [*Albert*, 2003; *Summers and Thorne*, 2003]. With the exception of very strong geomagnetic storms, the concentration of oxygen ions is believed to be very small, and therefore, we have decided to assume an oxygen fraction of 1 %O^+. During storm times, the hot O^+ concentration may increase substantially [*Daglis et al.*, 1999] but this is beyond the scope of our current capability.

Another method to estimate the He^+ concentration is to use the observed frequencies of EMIC waves. If the frequency of a hydrogen band wave is between the helium ion cyclotron frequency (f_{cHe}) and the so-called crossover frequency (f_{cr}), EMIC waves are right-hand polarized for parallel propagation [*Horne and Thorne*, 1993], and above f_{cr} the waves are left-hand polarized. Theory shows that EMIC waves are generated as left-hand polarized waves near the equator and furthermore that it is very difficult to generate right polarized waves, since very high resonant energies are required [*Kozyra et al.*, 1984]. Assuming a H^+–He^+ plasma and neglecting O^+, which is very small in our case, the crossover frequency can be estimated as

$$f_{cr}/f_{cp} = 1/4 \cdot \sqrt{1 + 15\eta}$$

where η is the ratio of the helium to the total number density and thereby defining the helium fraction. Since the crossover frequency depends on the concentration of helium ions, it is possible to estimate the ion composition based on observations of f_{cr}, below which no EMIC waves should be present.

As shown in Figure 2 hydrogen band EMIC wave events are observed with peak frequencies down to about $0.28f_{cp}$. Taking the frequency width into account, using the above equation, one can derive a helium fraction between 2 and 3%. However, most of the waves can be found above $0.28f_{cp}$; therefore, 2–3% acts as a minimum for the He^+ fraction. The peak frequency of hydrogen band waves ($f_m = 0.4f_{cp}$) leads to a He^+ concentration of about 10%. As a compromise, we decided to assume a He^+ fraction of 5% and as a consequence 94% H^+ and 1% O^+ ions.

3.2.5. Latitudinal Distribution

EMIC waves are believed to be generated close to the magnetic equator and propagate along the magnetic field lines to higher latitudes. There is very little information about the latitudinal distribution of EMIC waves above 15° latitude, but since EMIC waves can be observed on the ground with a similar MLT distribution to

Table 1. Parameters of the EMIC Waves Nominal Model Used to Calculate the Pitch Angle Diffusion Rates Using the PADIE Code

Parameter	Hydrogen Band Waves	Helium Band Waves
B_W	1 nT	1 nT
f_m/f_{cp}	0.4	0.15
df/f_{cp}	0.02	0.02
f_{lc}/f_{cp}	$(f_m - 2df)/f_{cp} = 0.36$	$(f_m - 2df)/f_{cp} = 0.11$
f_{uc}/f_{cp}	$(f_m + 2df)/f_{cp} = 0.44$	$(f_m + 2df)/f_{cp} = 0.19$
f_{pe}/f_{ce}	10.0	
X_m	0.0	
X_w	tan 15°	
X_{cut}	$2 \cdot X_w$	
Latitude	All latitudes	
Resonances	$-10 \le n \le 10$	
Ion composition	94% H^+, 5% He^+, 1% O^+	

that in space although there can be significant differences [*Posch et al.*, 2010], we assume that the waves are present over all latitudes for the nominal model. To account for the change in Earth's magnetic field and thereby the change of the proton and electron cyclotron frequencies, the PADIE code adjusts all frequencies to the corresponding latitude at which the diffusion rates are calculated.

A summary of all parameters of the nominal EMIC wave model is shown in Table 1.

3.3. Wave Power

Since the EMIC wave data are sparse and in order to only model the significant wave power of EMIC waves, the wave power of each L^* sector was averaged over the whole afternoon sector (12–18 MLT) and set the wave power of all the other MLT sectors to zero. Inside the afternoon sector the time-averaged wave power B_w^2 was calculated by averaging the wave power over all times, including times without an EMIC wave event, and therefore, the average wave power is significantly lower than the wave power of a single event. Although previous theoretical calculations have used a peak power of 1 nT^2 [e.g., *Summers and Thorne*, 2003] and thereby suggest that the waves can cause strong diffusion, the bursty and sporadic nature of the waves suggests that strong diffusion is localized and the averaging done here means that it is not captured in our model. This is discussed further below.

The resulting average wave power of the nominal model for hydrogen and helium band waves, ranging from $L^* = 3.5$ to $L^* = 7.0$ for five levels of Kp is shown in Figure 3. Generally, the intensity of the helium band waves (solid line) is about one decade higher than the intensity of the hydrogen band waves (dotted line) and also the intensity is increasing with Kp for both bands. For $Kp > 3$ the intensity varies about one decade with L^* and becomes more variable at lower magnetic activities. This is due to the fact that there is very little data for lower magnetic activities ($Kp < 3$). For $Kp < 1$ nearly all available data were below the noise threshold, with only one value of the wave power in the helium band remaining. Since the trend in Kp suggests this value is an exception, we decided to set this value to zero, thereby leaving no wave power at all for all $Kp < 1$.

4. Diffusion Rates

4.1. Bounce-Averaged Diffusion Rates

To illustrate the energy dependence of the particle distribution, Figure 4 shows an example for bounce-averaged pitch angle diffusion coefficients calculated using the PADIE code for hydrogen band (left) and helium band EMIC waves (right) at $L^* = 4.5$ and $Kp > 4$ and also the strong diffusion rate as given in *Summers and Thorne* [2003] at an energy of 10 MeV. In the case of hydrogen band waves, the diffusion rates extend from the loss cone, which at this location is typically about 4°, up to larger equatorial pitch angles. The pitch angle at which the diffusion rates drop to zero increases with energy from about 45° for 5.5 MeV to 60° for 10.0 MeV. This suggests that electrons can be diffused into the loss cone and lost into the atmosphere by EMIC waves, but since the diffusion rates do not extend all the way to 90°, electrons at large pitch angles will not be effectively scattered by EMIC waves and should remain trapped in the magnetosphere. At higher energies of 20–30 MeV the diffusion rates near the loss cone are much smaller; therefore, the losses

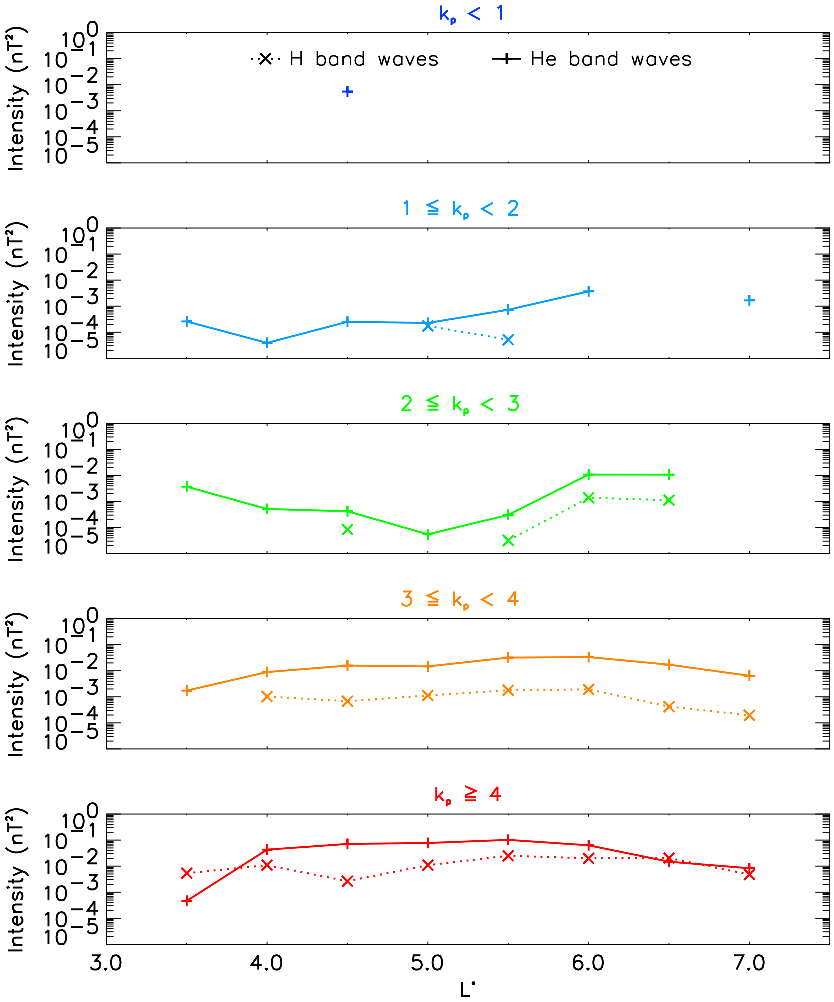

Figure 3. Time-averaged wave intensity versus L^* for hydrogen and helium band EMIC waves for different levels of Kp for the region of 12–18 MLT.

caused by EMIC waves should be a lot lower. Furthermore, the pitch angle at which the diffusion rates drop to zero is further increased but still does not extend all the way to 90°.

In contrast to the hydrogen band EMIC diffusion rates, helium band EMIC waves are effective at diffusing electrons at higher energies of about 9–30 MeV and the diffusion rates are not of the same order of magnitude as hydrogen band waves, since they differ by about two decades. They increase in energy and are peaked between 10 and 20 MeV, whereas hydrogen band diffusion rates are peaked near 5.5 MeV.

Figure 5 illustrates the relative importance of the bounce-averaged pitch angle, mixed pitch angle and energy, and energy diffusion rates at $L^* = 4.5$, $E = 10$ MeV, and $Kp > 4$. For hydrogen band waves, the energy diffusion coefficient is 5 orders of magnitude lower than the pitch angle diffusion. Helium band waves show no significant energy diffusion at $E = 10$ MeV and comparably small mixed pitch angle and energy diffusion. Therefore, we do not expect electron acceleration caused by EMIC waves.

4.2. Drift- and Bounce-Averaged Diffusion Rates

While only a few models such as the Salammbô and RAM model include a MLT resolution [*Jordanova et al.*, 2001], most models, including the BAS Radiation Belt Model, are based on data which is drift averaged over MLT. *Shprits et al.* [2009] have shown that MLT-averaged simulations can accurately predict the overall shape of the pitch angle distribution. Since in our model the wave power has been set to zero for all MLTs, except for the 6 h afternoon sector, computing the drift- and bounce-averaged diffusion coefficients is simply done by dividing the bounce-averaged diffusion rates of the afternoon sector by four.

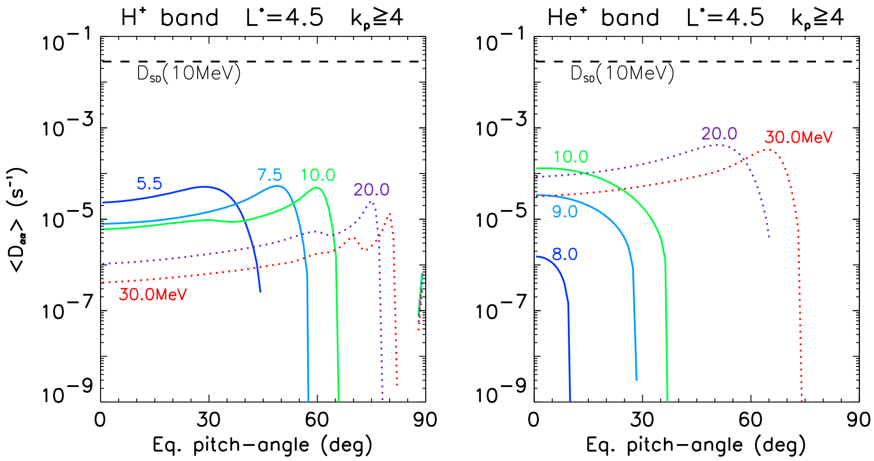

Figure 4. Bounce-averaged pitch angle diffusion rates for (left) hydrogen band and (right) helium band EMIC waves for different energies at $L^* = 4.5$ and wave amplitudes corresponding to $Kp \geq 4$ calculated using PADIE. Also shown is the strong diffusion rate (D_{SD}) for $E = 10$ MeV.

Figure 6 shows the drift- and bounce-averaged pitch angle (a–c) and energy diffusion rates (d–e) for all energy levels ranging from 100 eV to 10 MeV and all five levels of *Kp*. The diffusion rates were calculated based on the global EMIC wave model using PADIE. For comparison, we also show the hydrogen and helium band EMIC wave diffusion rates combined with the drift- and bounce-averaged pitch angle and energy diffusion coefficients caused by upper and lower band chorus waves as presented in *Horne et al.* [2013].

Most importantly, pitch angle diffusion due to EMIC waves is strongest at energies greater than about 2 MeV. There is also a very narrow region of high pitch angle diffusion rates very close to 90°. The pitch angle diffusion rates caused by hydrogen band and helium band EMIC waves both overall increase with *Kp* and are of the same order of magnitude, but the hydrogen band waves cause pitch angle diffusion down to lower energies of about 2 MeV, whereas the diffusion caused by helium band waves start at energies greater than 6 MeV. Since our data do not provide wave power for hydrogen band EMIC events at low magnetic activities, there is no pitch angle diffusion for $Kp < 2$.

In contrast to EMIC waves, the pitch-angle diffusion rates due to lower and upper band chorus (Figure 6c) extend over the whole range of energies. Near the loss cone, the diffusion due to chorus tends to be largest at lower energies between about 1 and 100 keV, whereas at large pitch angles the same level of diffusion shifts to higher energies. There is a minimum in the diffusion rates at small pitch angles, which lies between

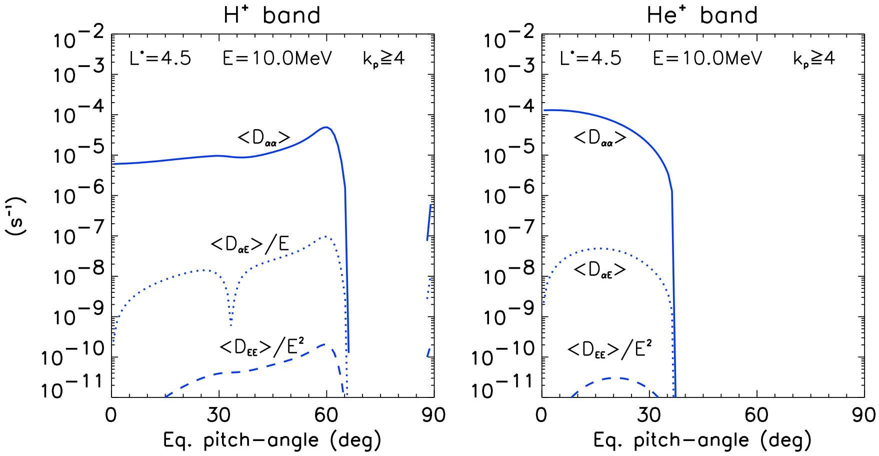

Figure 5. Bounce-averaged pitch angle, energy, and mixed pitch angle and energy diffusion coefficient at $L^* = 4.5$ and $E = 10$ MeV for (left) hydrogen band and (right) helium band EMIC waves.

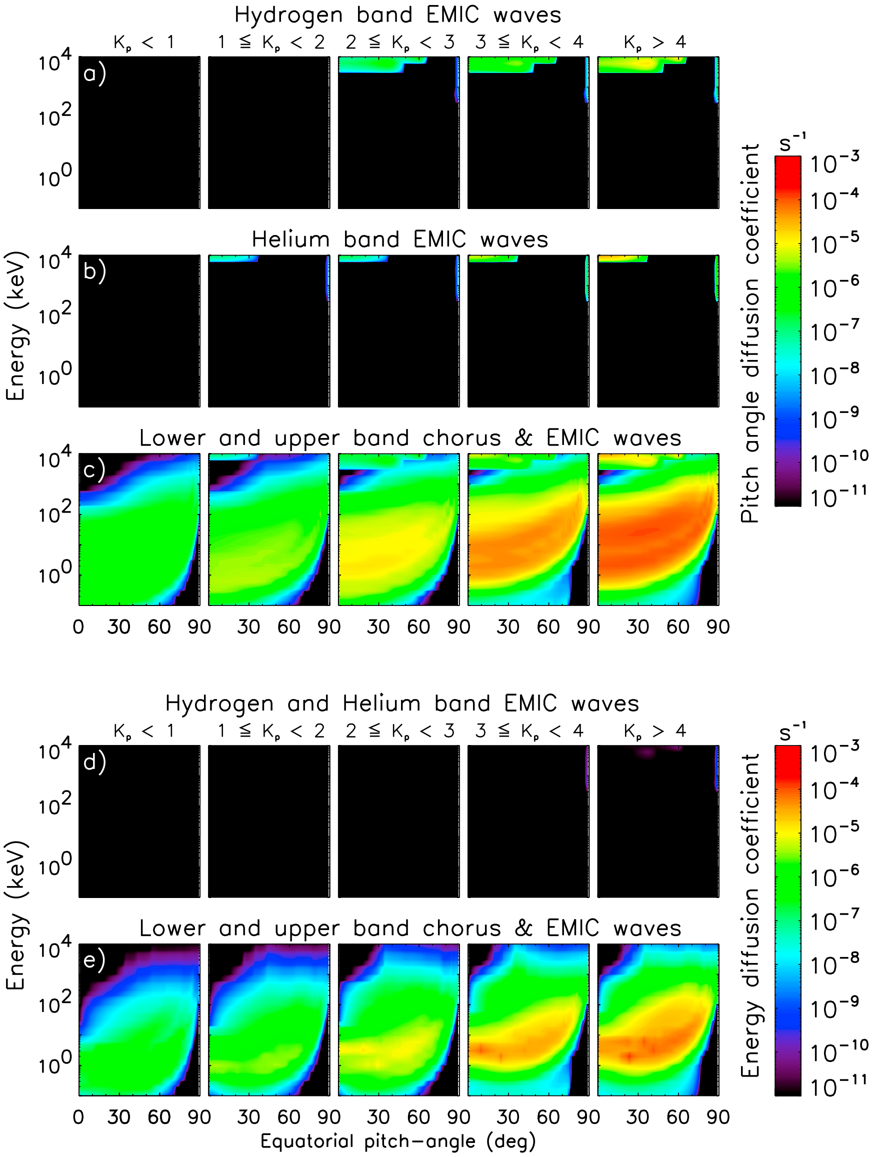

Figure 6. (a–c) The drift- and bounce-averaged pitch angle diffusion coefficients at $L^* = 4.5$ for five levels of Kp, caused by only hydrogen band in Figure 6a, helium band EMIC waves in Figure 6b, and all EMIC waves combined with upper and lower band chorus in Figure 6c. (d and e) The drift- and bounce-averaged energy diffusion coefficients, each for EMIC waves only and EMIC and combined upper and lower band chorus.

the ones due to chorus at lower energies and EMIC waves at higher energies, whereas the diffusion due to chorus and EMIC waves begins to merge at larger pitch angles.

There is no significant energy diffusion due to EMIC waves at all, except for pitch angles close to 90° and $Kp > 4$, whereas the energy diffusion due to chorus varies over the whole range of pitch angles and energies (Figures 6d and 6e).

5. Global Simulations

It has been shown by *Albert and Young* [2005] and *Subbotin et al.* [2010] that the effect of the cross diffusion terms $D_{\alpha E}$ and $D_{E\alpha}$ on equatorially mirroring particles is small. On the other hand, *Tao et al.* [2008, 2009] have shown that they may have a significant effect, which increases with particle energy and becomes important for energies greater than about 2 MeV and equatorial pitch angles below 60°. Therefore, although we are using a different chorus model, the omission of cross diffusion terms in our model could be important.

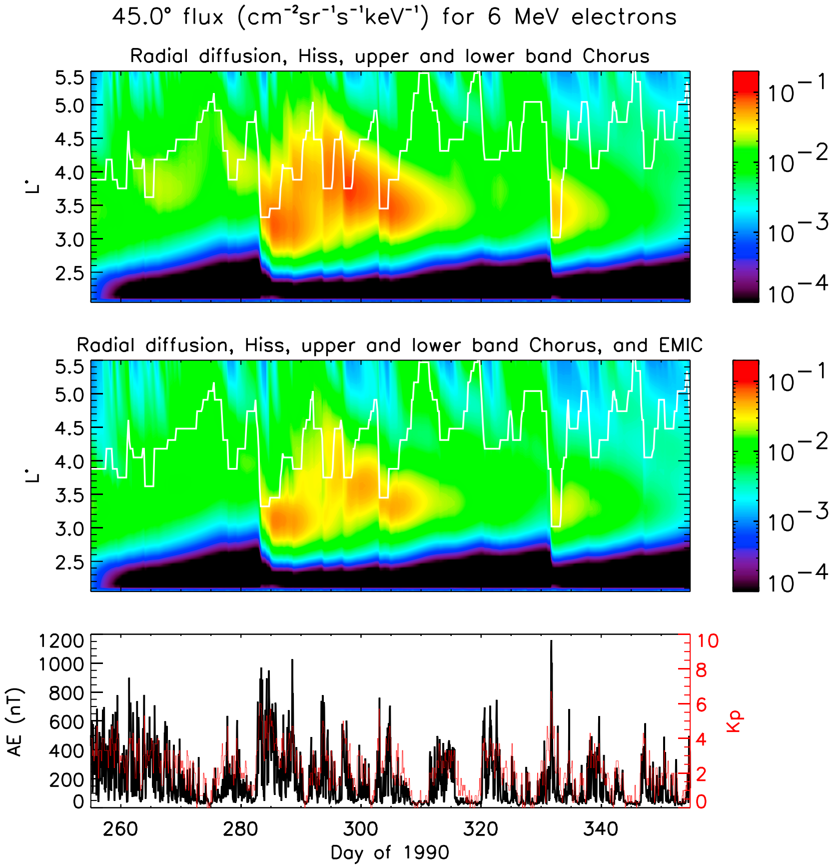

Figure 7. Temporal distribution of the flux of 6 MeV electrons with an equatorial pitch angle of 45° as a function of L^* calculated by the BAS Radiation Belt Model driven by (top) radial diffusion, hiss, and combined upper and lower band chorus and (middle) additionally by hydrogen and helium band EMIC waves. The plasmapause location is indicated by the white line. (bottom) The geomagnetic activity, as monitored by the *AE* and *Kp* indices.

However, since we are comparing simulations with and without EMIC waves, the results should still show at which energies and pitch angle EMIC waves are important.

To assess the importance of EMIC waves on a global scale, the BAS Radiation Belt Model was run for energies up to 10 MeV for a 100 day period in 1990, which is a period that has already been studied for chorus, but not for EMIC waves [e.g., *Glauert et al.*, 2014]. Figure 7 (top) shows the flux of electrons with an equatorial pitch angle of 45° caused by radial diffusion, hiss, and combined upper and lower band chorus for 6 MeV electrons driven by the *Kp* index, which is shown in Figure 7 (bottom).

During the initial period there are small variations in the electron flux near $L^* = 4$, and the slot region increases from about $L^* = 2.5$ at the beginning of the run to about $L^* = 3.0$ at day 255. There is a major increase in the flux and the *Kp* and *AE* indices at day 285. The outer boundary of the flux begins to move inward around day 290, and the flux is reduced to its initial moderate levels at around day 315. There is a further small increase in the flux at day 322 also associated with a rapid increase of *Kp* and *AE*. Each increase of the flux is also associated with the plasmapause rapidly moving to lower L^*, since chorus waves are mainly seen outside the plasmapause.

It is interesting to note that our simulations suggest that the combination of chorus waves and radial diffusion can accelerate electrons to energies greater than 6 MeV at pitch angles of 45°. *Li et al.* [2014] have suggested that chorus can accelerate electrons locally to energies of the order of 6 MeV. In contrast, simulations by *Shprits et al.* [2013] show that the chorus waves might not, at least directly, contribute to the acceleration at 6 MeV. Therefore, we have performed additional simulations, where we have set the chorus energy diffusion rates to zero for $E \geq 4$ MeV. In this case, the electron flux is barely reduced compared to the original simulations, which suggests that the 6 MeV electrons in our simulations near $3 < L^* < 4$

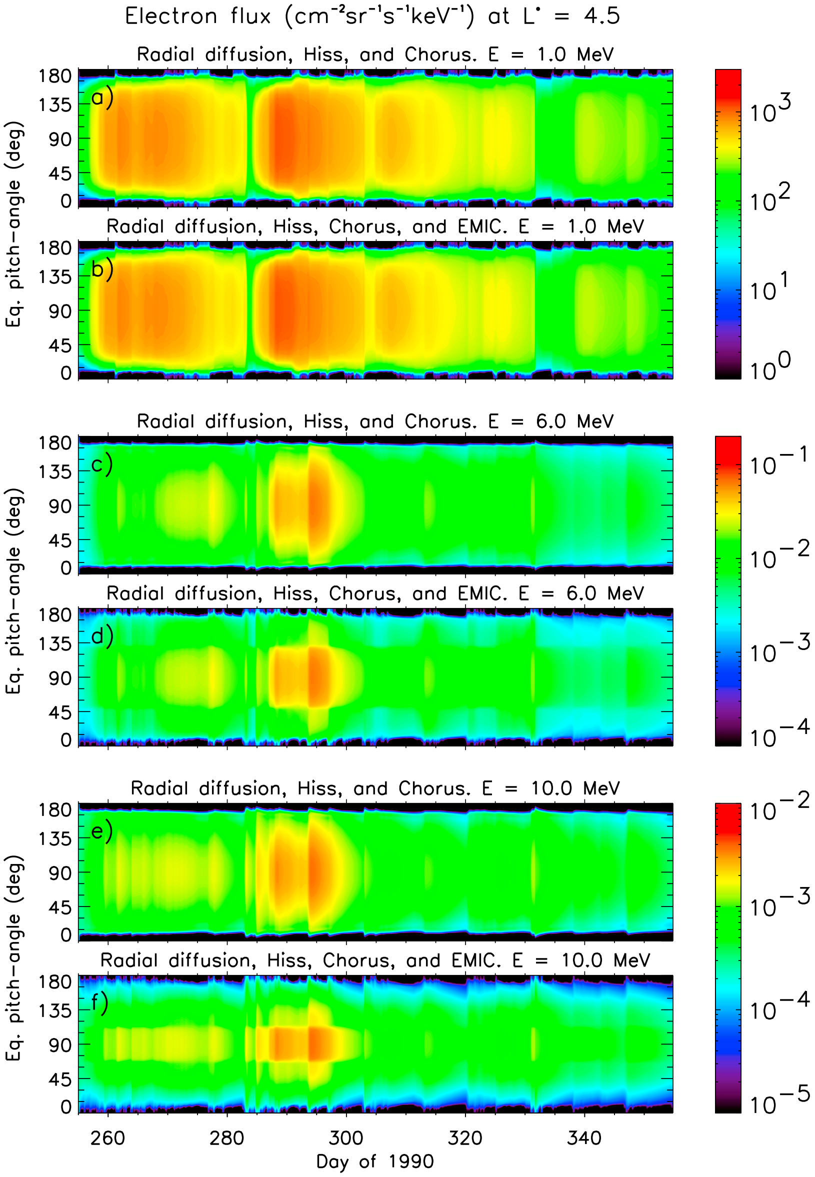

Figure 8. (a–f) Equatorial pitch angle dependence of the electron flux at $L^* = 4.5$ for three different energies calculated using the BAS Radiation Belt Model during a 100 day period of the year 1990. The simulations in panels a, c, and e were driven by radial diffusion, hiss, and combined upper and lower band chorus, while the simulations in panels b, d, and f were driven by radial diffusion, hiss, and combined upper and lower band chorus and additionally hydrogen and helium band EMIC waves.

were initially accelerated by chorus at larger L^* and then accelerated again by radial diffusion as they were transported to lower L^*. The reason that *Li et al.* [2014] were able to obtain wave acceleration up to 6 MeV is that f_{pe}/f_{ce} was much lower in their case study than that used here, and thus, they could obtain resonance at higher energies. Our model uses an average value for f_{pe}/f_{ce} based on a statistical analysis of the waves which is higher than that used by Li et al. and tends to limit wave acceleration at the highest energies. Our model also includes a range of wave normal angles and diffusion due to multiple harmonic resonance as *Li et al.*'s [2014] does. We note, however, that there are other lower frequency chorus waves at frequencies below $0.1f_{ce}$ [*Meredith et al.*, 2014b] which are not currently included in our chorus model and which could affect this result.

To study the effect of hydrogen and helium EMIC waves on the electron flux, the same simulation was run again, this time with additional hydrogen and helium band EMIC diffusion rates. The EMIC rates result in a

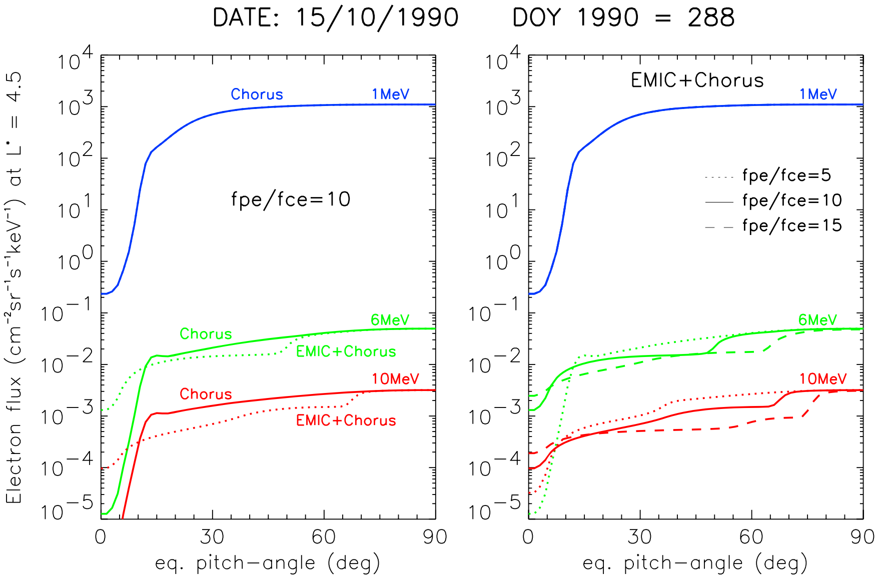

Figure 9. Pitch angle dependence of the electron flux at $L^* = 4.5$ for three different energies, calculated using the BAS Radiation Belt Model driven by radial diffusion, hiss, and combined upper and lower band chorus (solid line, labeled "Chorus") and additionally including hydrogen and helium band EMIC waves (dotted line). (left) The flux that was calculated with a ratio of $f_{pe}/f_{ce} = 10$. (right) The flux that includes radial diffusion, plasmaspheric hiss, lower and upper band chorus, and EMIC waves for different values of f_{pe}/f_{ce}.

drop of the 45° electron flux, especially significant during day 285 and 310 for $L^* > 3.5$, which is due to the fact that our EMIC wave model is only defined for $L^* > 3.5$.

The pitch angle dependence of electron flux at $L^* = 4.5$ is shown in Figure 8 for three fixed electron energies of $E = 1$ MeV (Figures 8a and 8b), $E = 6$ MeV (Figures 8c and 8d), and $E = 10$ MeV (Figures 8e and Figure 8f). The full range of pitch angles from 0° to 180° is shown by mirroring our results at 90°.

For electron energies of $E = 1$ MeV, there is no significant difference in the electron flux with and without EMIC waves. For energies of $E = 6$ MeV the electron flux is significantly reduced by EMIC waves for pitch angles between about 0° and 50°. The reduction is particularly pronounced for particles with $E = 10$ MeV, where the flux is reduced for pitch angles between about 0° and 75°.

Since there is no CRRES Medium Electron Sensor (MEA) data for the electron flux at very high energies, a comparison of the simulation and the data could not be done. The effects of EMIC waves on high-energy electrons have been investigated by *Usanova et al.* [2014] and are consistent with our findings. In future, we hope to exploit the Van Allen Probes data to further assess the role of the waves on the particles.

To illustrate the pitch angle dependence of the electron flux at the energy levels used before a slice through the day 288 of year 1990 is shown in Figure 9. When EMIC waves are included, the electron flux is reduced by about a factor of 2 at 6 MeV and about 5 at 10 MeV, but for lower electron energies, e.g., $E = 1$ MeV, EMIC waves do not have an effect on the electron flux. Furthermore, *Li et al.* [2007] and *Albert and Shprits* [2009] have shown that EMIC waves may indirectly increase the loss for all pitch angles by creating large gradients in pitch angle and thereby facilitating loss by hiss and chorus. A comparison between simulations with and without EMIC waves shows that in our case a reduction of up to about 15% is only noticeable at very large energies of about 10 MeV. It is also noteworthy that EMIC waves maintain an electron flux at very low pitch angles less than about 10°. Furthermore, EMIC waves increase the pitch angle diffusion rates close to the equator.

Figure 9 (right) shows the sensitivity of the pitch angle diffusion rates to the ratio of f_{pe}/f_{ce}. All simulations in Figure 9 (left) were calculated for $f_{pe}/f_{ce} = 10$, while Figure 9 (right) shows results for different values of f_{pe}/f_{ce}, i.e., $f_{pe}/f_{ce} = 5$ (dotted line), $f_{pe}/f_{ce} = 10$ (solid line), and $f_{pe}/f_{ce} = 15$ (dashed line). There is still the same trend in energy, but the drop in pitch angle extends to higher pitch angles, while the ratio of f_{pe}/f_{ce}

increases. At energies greater than about 6 MeV an increase of f_{pe}/f_{ce} reduces the electron flux. Again, there is no significant difference at $E = 1$ MeV.

6. Discussion

The results and model presented here are based on the CRRES measurements of EMIC wave events. Since, depending on the location and magnetic activity, the data are sparse, the model has uncertainties to some extent. In order to understand the influence of the uncertainties of the different model parameters, we have done additional sensitivity tests, which are not shown here. We found that an increase in the frequency width or the peak position of the Gaussian extends pitch angle and energy diffusion up to higher pitch angles but still not all the way up to 90°. For instance, for $E = 5$ MeV electrons at $L^* = 4.5$ when the peak frequency f_m/f_{cp} was varied from 0.3 to 0.55, keeping all other parameters of the nominal model fixed, the diffusion rates extended from the loss cone up to 17° and 60°, respectively. Similarly, when only the frequency width df/f_{cp} was varied between 0.01 and 0.04, the diffusion rates extended from the loss cone up to about 35° and 50°, respectively. Setting both the peak frequency and the width to its respective maximum value allows for pitch angle diffusion at energies as low as 2 MeV for hydrogen band waves and 3 MeV for helium band waves. This is due to the fact that increasing the peak frequency or frequency width in the resonance condition allows EMIC waves to resonate with particles of lower energies. Thus, assuming a wider Gaussian frequency spectrum and/or a higher peak frequency will allow EMIC waves to have an effect at energies lower than 5 MeV. We have chosen typical spectral properties based on observations which lead to little scattering below 4 MeV. However, individual events with frequencies very close to the helium ion cyclotron frequency [*Ukhorskiy et al.*, 2010] could scatter electrons at lower energies—but this would not be typical.

It has been shown by *Li et al.* [2014] and *Ukhorskiy et al.* [2010] that the scattering by EMIC waves is mostly determined by the upper cutoff frequency of the Gaussian frequency distribution. Since this parameter is not determined from the CRRES measurements, we performed sensitivity tests for the upper cutoff frequency. These showed that while there are only small changes in the maximum pitch angle at which hydrogen band EMIC waves are effective in scattering electrons into the loss cone, a change of the upper cutoff for the helium band EMIC waves will allow the waves to effectively scatter electrons at slightly higher pitch angles and also at lower energies. For instance, in the case of $E = 7.5$ MeV the maximum pitch angle increases from about 25° at $f_{uc} = 0.19f_{cp}$ to about 40° at $f_{uc} = 0.24f_{cp}$. This increase of the maximum pitch angle also allows helium band EMIC waves to still be effective at energies as low as $E = 6$ MeV, but the corresponding diffusion rates are lower than in the case of higher energies of the nominal model. To assess the importance of these results for the global model, we performed a 100 day model run similar to the previous runs, but with $f_{uc} = 0.24f_{cp}$, which showed that the electron flux is only reduced by a small amount by the higher upper cutoff frequency. Therefore, the choice of the upper cutoff frequency used in the nominal model is sufficient. We note that our results are less sensitive to the choice of the upper cutoff due to the fact that the peak helium band frequency determined here is lower than that used in *Li et al.* [2014] and hence further from the helium ion cyclotron frequency.

As mentioned in section 3.2.2, we assume a value of $f_{pe}/f_{ce} = 10$. For hydrogen band waves f_{pe}/f_{ce} is of the order of 10, but for helium band waves f_{pe}/f_{ce} is around 15. Since the CRRES measurements indicate that the ratio of f_{pe}/f_{ce} for helium band waves might be higher than the value we assumed in our model, we have done sensitivity tests to understand the influence of the ratio of f_{pe}/f_{ce}, which are again not shown here. The results show that an increase of the ratio of f_{pe}/f_{ce} from 10 to 15 for hydrogen band waves at $L^* = 4.5$ and $E = 5.5$ MeV lowers the pitch angle diffusion rate by less than 1 order of magnitude. Furthermore, the diffusion rates extend from the loss cone up to about 45° and 60° as f_{pe}/f_{ce} increases. For helium band waves at $E = 10.0$ MeV an increase from $f_{pe}/f_{ce} = 10$ to 15 increases the diffusion rates by a factor of about 2, and the diffusion rates extend from the loss cone up to about 35° and 60°. For both, hydrogen and helium band waves, setting $f_{pe}/f_{ce} = 5$ at the before mentioned energies results in pitch angle diffusion rates that are at least 7 orders of magnitude lower than the ones at $f_{pe}/f_{ce} = 10$. In consequence, the model may underestimate the electron diffusion at lower energies of a few MeV especially for helium band waves and thus underestimate the losses.

Our simulations also neglect warm plasma effects which could affect the resonant energies allowing for EMIC waves to resonate with lower energies. These effects are likely to be most significant during geomagnetic storms [*Silin et al.*, 2011] particularly when the ring current is strong (low *Dst*). However, EMIC wave activity is more closely related to substorm activity and shows little correlation with *Dst* suggesting that warm plasma effect may not be so important, especially in the average sense.

Ground observations have shown that EMIC waves result in the precipitation of relativistic electrons with energies larger than a couple MeV [*Clilverd et al.*, 2007; *Millan et al.*, 2007; *Rodger et al.*, 2008] suggesting that they may play a role in the relativistic electron flux dropouts seen during the main phase of geomagnetic storms [e.g., *Blake et al.*, 2001; *Green et al.*, 2004]. However, satellite observations show no evidence for strong precipitation during the main phase of geomagnetic storms [*Horne et al.*, 2009; *Meredith et al.*, 2011; *Turner et al.*, 2012]. Our results show that, while EMIC waves can cause precipitation of relativistic electrons with energies greater than about 2 MeV near the loss cone, the bulk of the electron population with large pitch angles is not affected [*Usanova et al.*, 2014], and it therefore seems unlikely that EMIC waves alone are responsible for flux dropout events [*Turner et al.*, 2014a, 2014b].

EMIC waves usually appear in several short bursts that might cause strong diffusion locally. In our model, we have time averaged the wave power, including times when no EMIC waves were present, and applied the diffusion rates over the whole drift path of the electrons. The dashed line in Figure 4 shows the strong diffusion rate for 10 MeV electrons. The diffusion rates calculated using our model, which is based on time-averaged wave power, are about 3 orders of magnitude lower than the strong diffusion rate. In the companion paper *Meredith et al.* [2014a] show that the time-averaged intensity of the EMIC wave events measured by CRRES is about 30–50 times lower than the event-averaged intensity for helium and hydrogen band EMIC waves, respectively. Since the pitch angle diffusion coefficients scale linearly with the intensity, our model suggests that short bursts of EMIC events measured by CRRES cause diffusion rates that are at least one decade below the strong diffusion rate and are therefore unlikely to cause strong diffusion.

7. Conclusions

We have analyzed CRRES data to develop a global model for hydrogen and helium band EMIC waves. The resulting model covers the range between $L^* = 3.5$ and $L^* = 7.0$ between 12 and 18 MLT for five levels of *Kp* and all latitudes. The simulations based on our model were run for a period of 100 days in 1990. They show that EMIC waves can be a significant loss process for the high-energy electron flux with energies greater than about 2 MeV and equatorial pitch angles ranging from the loss cone up to about 60°, even using time-averaged EMIC wave power. We find that over time EMIC waves scatter all electrons with a pitch angle less than about 60° into the loss cone.

The distribution of electrons left behind in space looks like a pancake distribution, i.e., depleted between the loss cone and a pitch angle, that depends on the particle energy, and peaked between this angle up to 90°. At higher energies, the width of the pancake decreases. Since this effect only occurs for electron energies greater than about 2 MeV and the highest energy channel of the CRRES MEA instrument used in our earlier studies [*Glauert et al.*, 2014] measured the electron flux at $E = 1.582$ MeV, we cannot compare our simulations with CRRES measurements. But a recent study of the Van Allen Probes Relativistic Electron Proton Telescope (REPT) instrument data has shown that the loss of ultrarelativistic electrons caused by EMIC waves scattering is confined to pitch angles below about 45° [*Usanova et al.*, 2014], which supports the results predicted by our model.

Furthermore, our results suggest that EMIC waves, which only contribute to electron loss, are unlikely to set an upper limit on the energy of the flux of radiation belt electrons, because even at energies of 30 MeV and during periods of large geomagnetic activity they cannot remove particles close to 90°. The upper limit is an important issue in space weather research and for satellite design, as the spectrum of the particles needs to be taken into account when designing the shielding of electronic components. Further analysis of EMIC waves might enable us to specify an upper limit for the electron flux.

Acknowledgments
We thank Roger R. Anderson for providing the plasma frequencies used in this study. We also thank the NSSDC Omniweb for the provision of the *Kp* indices. This study is part of the British Antarctic Survey Polar Science for Planet Earth Programme. It was funded by the Natural Environment Research Council and additionally received funding from the European Union Seventh Framework Programme (FP7/2007-2013) under grant agreements 262468 (SPACECAST) and 284520 (MAARBLE). The Australian research contributing to these results has received funding from the Australian Research Council under project grant DP0222505 and linkage grant LX0882515. The data used to generate the plots in this paper are stored at the BAS Polar Data Centre and are available on request.

Michael Balikhin thanks the reviewers for their assistance in evaluating this paper.

References

Albert, J., and Y. Shprits (2009), Estimates of lifetimes against pitch angle diffusion, *J. Atmos. Sol. Terr. Phys.*, *71*(16), 1647–1652, doi:10.1016/j.jastp.2008.07.004.

Albert, J. M. (2003), Evaluation of quasi-linear diffusion coefficients for EMIC waves in a multispecies plasma, *J. Geophys. Res.*, *108*(A6), 1249, doi:10.1029/2002JA009792.

Albert, J. M. (2010), Diffusion by one wave and by many waves, *J. Geophys. Res.*, *115*, A00F05, doi:10.1029/2009JA014732.

Albert, J. M., and S. L. Young (2005), Multidimensional quasi-linear diffusion of radiation belt electrons, *Geophys. Res. Lett.*, *32*, L14110, doi:10.1029/2005GL023191.

Albert, J. M., N. P. Meredith, and R. B. Horne (2009), Three-dimensional diffusion simulation of outer radiation belt electrons during the 9 October 1990 magnetic storm, *J. Geophys. Res.*, *114*, A09214, doi:10.1029/2009JA014336.

Anderson, B. J., R. E. Erlandson, and L. J. Zanetti (1992a), A statistical study of Pc 1–2 magnetic pulsations in the equatorial magnetosphere: 1. Equatorial occurrence distributions, *J. Geophys. Res.*, *97*(A3), 3075–3088, doi:10.1029/91JA02706.

Anderson, B. J., R. E. Erlandson, and L. J. Zanetti (1992b), A statistical study of Pc 1–2 magnetic pulsations in the equatorial magnetosphere: 2. Wave properties, *J. Geophys. Res.*, *97*(A3), 3089–3101, doi:10.1029/91JA02697.

Baker, D. N., J. B. Blake, R. W. Klebesadel, and P. R. Higbie (1986), Highly relativistic electrons in the Earth's outer magnetosphere: 1. Lifetimes and temporal history 1979–1984, *J. Geophys. Res.*, *91*(A4), 4265–4276, doi:10.1029/JA091iA04p04265.

Baker, D. N., et al. (2013), A long-lived relativistic electron storage ring embedded in Earth's outer Van Allen belt, *Science*, *340*(6129), 186–190, doi:10.1126/science.1233518.

Beutier, T., and D. Boscher (1995), A three-dimensional analysis of the electron radiation belt by the Salammbô code, *J. Geophys. Res.*, *100*(A8), 14,853–14,861, doi:10.1029/94JA03066.

Blake, J. B., R. S. Selesnick, D. N. Baker, and S. Kanekal (2001), Studies of relativistic electron injection events in 1997 and 1998, *J. Geophys. Res.*, *106*(A9), 19,157–19,168, doi:10.1029/2000JA003039.

Boardsen, S. A., D. L. Gallagher, D. A. Gurnett, W. K. Peterson, and J. L. Green (1992), Funnel-shaped, low-frequency equatorial waves, *J. Geophys. Res.*, *97*(A10), 14,967–14,976, doi:10.1029/92JA00827.

Boscher, D., and S. Bourdarie (2004), ONERA-DESP library v2.2, Toulouse-France.

Brautigam, D. H., and J. M. Albert (2000), Radial diffusion analysis of outer radiation belt electrons during the October 9, 1990, magnetic storm, *J. Geophys. Res.*, *105*(A1), 291–309, doi:10.1029/1999JA900344.

Clilverd, M. A., C. J. Rodger, R. M. Millan, J. G. Sample, M. Kokorowski, M. P. McCarthy, T. Ulich, T. Raita, A. J. Kavanagh, and E. Spanswick (2007), Energetic particle precipitation into the middle atmosphere triggered by a coronal mass ejection, *J. Geophys. Res.*, *112*, A12206, doi:10.1029/2007JA012395.

Cornwall, J. M., F. V. Coroniti, and R. M. Thorne (1970), Turbulent loss of ring current protons, *J. Geophys. Res.*, *75*(25), 4699–4709, doi:10.1029/JA075i025p04699.

Daglis, I. A., R. M. Thorne, W. Baumjohann, and S. Orsini (1999), The terrestrial ring current: Origin, formation, and decay, *Rev. Geophys.*, *37*(4), 407–438, doi:10.1029/1999RG900009.

Fok, M.-C., R. B. Horne, N. P. Meredith, and S. A. Glauert (2008), Radiation belt environment model: Application to space weather nowcasting, *J. Geophys. Res.*, *113*, A03S08, doi:10.1029/2007JA012558.

Friedel, R. H. W., S. Bourdarie, and T. E. Cayton (2005), Intercalibration of magnetospheric energetic electron data, *Space Weather*, *3*, S09B04, doi:10.1029/2005SW000153.

Glauert, S. A., and R. B. Horne (2005), Calculation of pitch angle and energy diffusion coefficients with the PADIE code, *J. Geophys. Res.*, *110*, A04206, doi:10.1029/2004JA010851.

Glauert, S. A., R. B. Horne, and N. P. Meredith (2014), Three-dimensional electron radiation belt simulations using the BAS Radiation Belt Model with new diffusion models for chorus, plasmaspheric hiss, and lightning-generated whistlers, *J. Geophys. Res. Space Physics*, *119*, 268–289, doi:10.1002/2013JA019281.

Green, J. C., T. G. Onsager, T. P. O'Brien, and D. N. Baker (2004), Testing loss mechanisms capable of rapidly depleting relativistic electron flux in the Earth's outer radiation belt, *J. Geophys. Res.*, *109*, A12211, doi:10.1029/2004JA010579.

Horne, R. B., and R. M. Thorne (1993), On the preferred source location for the convective amplification of ion cyclotron waves, *J. Geophys. Res.*, *98*(A6), 9233–9247, doi:10.1029/92JA02972.

Horne, R. B., and R. M. Thorne (1994), Convective instabilities of electromagnetic ion cyclotron waves in the outer magnetosphere, *J. Geophys. Res.*, *99*(A9), 17,259–17,273, doi:10.1029/94JA01259.

Horne, R. B., and R. M. Thorne (1998), Potential waves for relativistic electron scattering and stochastic acceleration during magnetic storms, *Geophys. Res. Lett.*, *25*(15), 3011–3014, doi:10.1029/98GL01002.

Horne, R. B., R. M. Thorne, S. A. Glauert, J. M. Albert, N. P. Meredith, and R. R. Anderson (2005a), Timescale for radiation belt electron acceleration by whistler mode chorus waves, *J. Geophys. Res.*, *110*, A03225, doi:10.1029/2004JA010811.

Horne, R. B., et al. (2005b), Wave acceleration of electrons in the Van Allen radiation belts, *Nature*, *437*(7056), 227–230.

Horne, R. B., N. P. Meredith, S. A. Glauert, A. Varotsou, D. Boscher, R. M. Thorne, Y. Y. Shprits, and R. R. Anderson (2006), *Mechanisms for the Acceleration of Radiation Belt Electrons, Geophys. Monogr. Ser.*, vol. 167, pp. 151–173, AGU, Washington, D. C.

Horne, R. B., R. M. Thorne, S. A. Glauert, N. P. Meredith, D. Pokhotelov, and O. Santolík (2007), Electron acceleration in the Van Allen radiation belts by fast magnetosonic waves, *Geophys. Res. Lett.*, *34*, L17107, doi:10.1029/2007GL030267.

Horne, R. B., M. M. Lam, and J. C. Green (2009), Energetic electron precipitation from the outer radiation belt during geomagnetic storms, *Geophys. Res. Lett.*, *36*, L19104, doi:10.1029/2009GL040236.

Horne, R. B., T. Kersten, S. A. Glauert, N. P. Meredith, D. Boscher, A. Sicard-Piet, R. M. Thorne, and W. Li (2013), A new diffusion matrix for whistler mode chorus waves, *J. Geophys. Res. Space Physics*, *118*, 6302–6318, doi:10.1002/jgra.50594.

Jordanova, V. K., C. J. Farrugia, R. M. Thorne, G. V. Khazanov, G. D. Reeves, and M. F. Thomsen (2001), Modeling ring current proton precipitation by electromagnetic ion cyclotron waves during the May 14–16, 1997, storm, *J. Geophys. Res.*, *106*(A1), 7–22, doi:10.1029/2000JA002008.

Jordanova, V. K., J. Albert, and Y. Miyoshi (2008), Relativistic electron precipitation by EMIC waves from self-consistent global simulations, *J. Geophys. Res.*, *113*, A00A10, doi:10.1029/2008JA013239.

Katoh, Y., and Y. Omura (2007), Computer simulation of chorus wave generation in the Earth's inner magnetosphere, *Geophys. Res. Lett.*, *34*, L03102, doi:10.1029/2006GL028594.

Kozyra, J. U., T. E. Cravens, A. F. Nagy, E. G. Fontheim, and R. S. B. Ong (1984), Effects of energetic heavy ions on electromagnetic ion cyclotron wave generation in the plasmapause region, *J. Geophys. Res.*, *89*(A4), 2217–2233, doi:10.1029/JA089iA04p02217.

Li, W., Y. Y. Shprits, and R. M. Thorne (2007), Dynamic evolution of energetic outer zone electrons due to wave-particle interactions during storms, *J. Geophys. Res.*, *112*, A10220, doi:10.1029/2007JA012368.

Li, W., R. M. Thorne, N. P. Meredith, R. B. Horne, J. Bortnik, Y. Y. Shprits, and B. Ni (2008), Evaluation of whistler mode chorus amplification during an injection event observed on CRRES, *J. Geophys. Res.*, *113*, A09210, doi:10.1029/2008JA013129.

Li, W., J. Bortnik, R. M. Thorne, and V. Angelopoulos (2011), Global distribution of wave amplitudes and wave normal angles of chorus waves using THEMIS wave observations, *J. Geophys. Res.*, *116*, A12205, doi:10.1029/2011JA017035.

Li, W., et al. (2014), Radiation belt electron acceleration by chorus waves during the 17 March 2013 storm, *J. Geophys. Res. Space Physics*, *119*, 4681–4693, doi:10.1002/2014JA019945.

Lorentzen, K. R., J. B. Blake, U. S. Inan, and J. Bortnik (2001), Observations of relativistic electron microbursts in association with VLF chorus, *J. Geophys. Res.*, *106*(A4), 6017–6027, doi:10.1029/2000JA003018.

Lyons, L. R., and R. M. Thorne (1973), Equilibrium structure of radiation belt electrons, *J. Geophys. Res.*, *78*(13), 2142–2149, doi:10.1029/JA078i013p02142.

Ma, Q., W. Li, R. M. Thorne, and V. Angelopoulos (2013), Global distribution of equatorial magnetosonic waves observed by THEMIS, *Geophys. Res. Lett.*, *40*, 1895–1901, doi:10.1002/grl.50434.

McCollough, J. P., J. L. Gannon, D. N. Baker, and M. Gehmeyr (2008), A statistical comparison of commonly used external magnetic field models, *Space Weather*, *6*, S10001, doi:10.1029/2008SW000391.

Meredith, N. P., R. B. Horne, and R. R. Anderson (2001), Substorm dependence of chorus amplitudes: Implications for the acceleration of electrons to relativistic energies, *J. Geophys. Res.*, *106*(A7), 13,165–13,178, doi:10.1029/2000JA900156.

Meredith, N. P., R. M. Thorne, R. B. Horne, D. Summers, B. J. Fraser, and R. R. Anderson (2003), Statistical analysis of relativistic electron energies for cyclotron resonance with EMIC waves observed on CRRES, *J. Geophys. Res.*, *108*(A6), 1250, doi:10.1029/2002JA009700.

Meredith, N. P., R. B. Horne, R. M. Thorne, D. Summers, and R. R. Anderson (2004), Substorm dependence of plasmaspheric hiss, *J. Geophys. Res.*, *109*, A06209, doi:10.1029/2004JA010387.

Meredith, N. P., R. B. Horne, S. A. Glauert, R. M. Thorne, D. Summers, J. M. Albert, and R. R. Anderson (2006), Energetic outer zone electron loss timescales during low geomagnetic activity, *J. Geophys. Res.*, *111*, A05212, doi:10.1029/2005JA011516.

Meredith, N. P., R. B. Horne, S. A. Glauert, and R. R. Anderson (2007), Slot region electron loss timescales due to plasmaspheric hiss and lightning-generated whistlers, *J. Geophys. Res.*, *112*, A08214, doi:10.1029/2007JA012413.

Meredith, N. P., R. B. Horne, and R. R. Anderson (2008), Survey of magnetosonic waves and proton ring distributions in the Earth's inner magnetosphere, *J. Geophys. Res.*, *113*, A06213, doi:10.1029/2007JA012975.

Meredith, N. P., R. B. Horne, S. A. Glauert, D. N. Baker, S. G. Kanekal, and J. M. Albert (2009), Relativistic electron loss timescales in the slot region, *J. Geophys. Res.*, *114*, A03222, doi:10.1029/2008JA013889.

Meredith, N. P., R. B. Horne, M. M. Lam, M. H. Denton, J. E. Borovsky, and J. C. Green (2011), Energetic electron precipitation during high-speed solar wind stream driven storms, *J. Geophys. Res.*, *116*, A05223, doi:10.1029/2010JA016293.

Meredith, N. P., R. B. Horne, A. Sicard-Piet, D. Boscher, K. H. Yearby, W. Li, and R. M. Thorne (2012), Global model of lower band and upper band chorus from multiple satellite observations, *J. Geophys. Res.*, *117*, A10225, doi:10.1029/2012JA017978.

Meredith, N. P., R. B. Horne, T. Kersten, B. J. Fraser, and R. S. Grew (2014a), Global morphology and spectral properties of EMIC waves derived from CRRES observations, *J. Geophys. Res. Space Physics*, *119*, 5328–5342, doi:10.1002/2014JA020064.

Meredith, N. P., R. B. Horne, W. Li, R. M. Thorne, and A. Sicard-Piet (2014b), Global model of low-frequency chorus (flhr < f < 0.1fce) from multiple satellite observations, *Geophys. Res. Lett.*, *41*, 280–286, doi:10.1002/2013GL059050.

Millan, R. M., R. P. Lin, D. M. Smith, and M. P. McCarthy (2007), Observation of relativistic electron precipitation during a rapid decrease of trapped relativistic electron flux, *Geophys. Res. Lett.*, *34*, L10101, doi:10.1029/2006GL028653.

Nishimura, Y., et al. (2010), Identifying the driver of pulsating aurora, *Science*, *330*(6000), 81–84, doi:10.1126/science.1193186.

Olson, W. P., and K. A. Pfitzer (1977), Magnetospheric magnetic field modeling, annual scientific report, Air Force Office of Sci. Res., 96 pp., McDonnell Douglas Astronaut. Co., Huntington Beach, Calif.

Omura, Y., M. Hikishima, Y. Katoh, D. Summers, and S. Yagitani (2009), Nonlinear mechanisms of lower-band and upper-band VLF chorus emissions in the magnetosphere, *J. Geophys. Res.*, *114*, A07217, doi:10.1029/2009JA014206.

Paulikas, G. A., and J. B. Blake (1979), *Effects of the Solar Wind on Magnetospheric Dynamics: Energetic Electrons at the Synchronous Orbit*, *Geophys. Monogr. Ser.*, vol. 21, pp. 180–202, AGU, Washington, D. C.

Posch, J. L., M. J. Engebretson, M. T. Murphy, M. H. Denton, M. R. Lessard, and R. B. Horne (2010), Probing the relationship between electromagnetic ion cyclotron waves and plasmaspheric plumes near geosynchronous orbit, *J. Geophys. Res.*, *115*, A11205, doi:10.1029/2010JA015446.

Reeves, G. D., et al. (2013), Electron acceleration in the heart of the Van Allen radiation belts, *Science*, *341*(6149), 991–994, doi: 10.1126/science.1237743.

Rodger, C. J., T. Raita, M. A. Clilverd, A. Seppälä, S. Dietrich, N. R. Thomson, and T. Ulich (2008), Observations of relativistic electron precipitation from the radiation belts driven by EMIC waves, *Geophys. Res. Lett.*, *35*, L16106, doi:10.1029/2008GL034804.

Santolík, O., C. A. Kletzing, W. S. Kurth, G. B. Hospodarsky, and S. R. Bounds (2014), Fine structure of large-amplitude chorus wave packets, *Geophys. Res. Lett.*, *41*, 293–299, doi:10.1002/2013GL058889.

Shprits, Y. Y., R. M. Thorne, R. Friedel, G. D. Reeves, J. Fennell, D. N. Baker, and S. G. Kanekal (2006), Outward radial diffusion driven by losses at magnetopause, *J. Geophys. Res.*, *111*, A11214, doi:10.1029/2006JA011657.

Shprits, Y. Y., L. Chen, and R. M. Thorne (2009), Simulations of pitch angle scattering of relativistic electrons with MLT-dependent diffusion coefficients, *J. Geophys. Res.*, *114*, A03219, doi:10.1029/2008JA013695.

Shprits, Y. Y., D. Subbotin, A. Drozdov, M. E. Usanova, A. Kellerman, K. Orlova, D. N. Baker, D. L. Turner, and K.-C. Kim (2013), Unusual stable trapping of the ultrarelativistic electrons in the Van Allen radiation belts, *Nat. Phys.*, *9*(11), 699–703, doi:10.1038/nphys2760.

Silin, I., I. R. Mann, R. D. Sydora, D. Summers, and R. L. Mace (2011), Warm plasma effects on electromagnetic ion cyclotron wave MeV electron interactions in the magnetosphere, *J. Geophys. Res.*, *116*, A05215, doi:10.1029/2010JA016398.

Su, Z., F. Xiao, H. Zheng, and S. Wang (2010), STEERB: A three-dimensional code for storm-time evolution of electron radiation belt, *J. Geophys. Res.*, *115*, A09208, doi:10.1029/2009JA015210.

Subbotin, D., Y. Shprits, and B. Ni (2010), Three-dimensional VERB radiation belt simulations including mixed diffusion, *J. Geophys. Res.*, *115*, A03205, doi:10.1029/2009JA015070.

Subbotin, D. A., and Y. Y. Shprits (2009), Three-dimensional modeling of the radiation belts using the Versatile Electron Radiation Belt (VERB) code, *Space Weather*, *7*, S10001, doi:10.1029/2008SW000452.

Summers, D., and R. M. Thorne (2003), Relativistic electron pitch-angle scattering by electromagnetic ion cyclotron waves during geomagnetic storms, *J. Geophys. Res.*, *108*(A4), 943–946, doi:10.1029/2002JA009489.

Summers, D., R. M. Thorne, and F. Xiao (1998), Relativistic theory of wave-particle resonant diffusion with application to electron acceleration in the magnetosphere, *J. Geophys. Res.*, *103*(A9), 20,487–20,500, doi:10.1029/98JA01740.

Summers, D., B. Ni, and N. P. Meredith (2007), Timescales for radiation belt electron acceleration and loss due to resonant wave-particle interactions: 1. Theory, *J. Geophys. Res.*, *112*, A04206, doi:10.1029/2006JA011801.

Tao, X., A. A. Chan, J. M. Albert, and J. A. Miller (2008), Stochastic modeling of multidimensional diffusion in the radiation belts, *J. Geophys. Res.*, *113*, A07212, doi:10.1029/2007JA012985.

Tao, X., J. M. Albert, and A. A. Chan (2009), Numerical modeling of multidimensional diffusion in the radiation belts using layer methods, *J. Geophys. Res.*, *114*, A02215, doi:10.1029/2008JA013826.

Tao, X., J. Bortnik, J. M. Albert, and R. M. Thorne (2012), Comparison of bounce-averaged quasi-linear diffusion coefficients for parallel propagating whistler mode waves with test particle simulations, *J. Geophys. Res.*, *117*, A10205, doi:10.1029/2012JA017931.

Thorne, R. M., B. Ni, X. Tao, R. B. Horne, and N. P. Meredith (2010), Scattering by chorus waves as the dominant cause of diffuse auroral precipitation, *Nature*, *467*(7318), 943–946.

Turner, D. L., Y. Shprits, M. Hartinger, and V. Angelopoulos (2012), Explaining sudden losses of outer radiation belt electrons during geomagnetic storms, *Nat. Phys.*, *8*(3), 208–212.

Turner, D. L., et al. (2014a), On the cause and extent of outer radiation belt losses during the 30 September 2012 dropout event, *J. Geophys. Res. Space Physics*, *119*, 1530–1540, doi:10.1002/2013JA019446.

Turner, D. L., et al. (2014b), Competing source and loss mechanisms due to wave-particle interactions in Earth's outer radiation belt during the 30 September to 3 october 2012 geomagnetic storm, *J. Geophys. Res. Space Physics*, *119*, 1960–1979, doi:10.1002/2014JA019770.

Ukhorskiy, A. Y., Y. Y. Shprits, B. J. Anderson, K. Takahashi, and R. M. Thorne (2010), Rapid scattering of radiation belt electrons by storm-time EMIC waves, *Geophys. Res. Lett.*, *37*, L09101, doi:10.1029/2010GL042906.

Usanova, M. E., I. R. Mann, J. Bortnik, L. Shao, and V. Angelopoulos (2012), THEMIS observations of electromagnetic ion cyclotron wave occurrence: Dependence on AE, SYMH, and solar wind dynamic pressure, *J. Geophys. Res.*, *117*, A10218, doi:10.1029/2012JA018049.

Usanova, M. E., et al. (2014), Effect of EMIC waves on relativistic and ultrarelativistic electron populations: Ground-based and Van Allen probes observations, *Geophys. Res. Lett.*, *41*, 1375–1381, doi:10.1002/2013GL059024.

Varotsou, A., D. Boscher, S. Bourdarie, R. B. Horne, S. A. Glauert, and N. P. Meredith (2005), Simulation of the outer radiation belt electrons near geosynchronous orbit including both radial diffusion and resonant interaction with whistler-mode chorus waves, *Geophys. Res. Lett.*, *32*, L19106, doi:10.1029/2005GL023282.